[18]Dipartimento di Matematica e Fisica, Universita degli Studi Roma Tre, Via della Vasca Navale 84, 00146 Roma, Italy.
[19]Istituto Nazionale di Fisica Nucleare, Sezione di Torino, Via Pietro Giuria 1, 10125 Torino, Italy.
[20]Dipartimento di Fisica, Universita degli Studi di Torino, Via Pietro Giuria 1, 10125 Torino, Italy.
[21]INAF Osservatorio Astro sico di Arcetri, Largo Enrico Fermi 5, 50125 Firenze, Italy.
[22]Dipartimento di Fisica e Astronomia, Universita degli Studi di Firenze, Via Sansone 1, 50019 Sesto Fiorentino (FI), Italy.
[23]Istituto Nazionale di Fisica Nucleare, Sezione di Firenze, Via Sansone 1, 50019 Sesto Fiorentino (FI), Italy.
[24]ASI -Agenzia Spaziale Italiana, Via del Politecnico snc, 00133 Roma, Italy.
[25]Istituto Nazionale di Fisica Nucleare, Sezione di Roma "Tor Vergata", Via della Ricerca Scienti ca 1, 00133 Roma, Italy.
[26]Department of Physics and Kavli Institute for Particle Astrophysics and Cosmology, Stanford University, Stanford, California 94305, USA.
[27]Astronomical Institute of the Czech Academy of Sciences, Boc n II 1401/1, 14100 Praha 4, Czech Republic.
[28]RIKEN Cluster for Pioneering Research, 2-1 Hirosawa, Wako, Saitama 351-0198, Japan.
[29]California Institute of Technology, Pasadena, CA 91125, USA.
[30]Yamagata University,1-4-12 Kojirakawa-machi, Yamagata-shi 990-8560, Japan.
[31]Osaka University, 1-1 Yamadaoka, Suita, Osaka 565-0871, Japan.
[32]Department of Physics, Faculty of Science and Engineering, Chuo University, 1-13-27 Kasuga, Bunkyo-ku, Tokyo 112-8551, Japan.
[33]Institute for Astrophysical Research, Boston University, 725 Commonwealth Avenue, Boston, MA 02215, USA.
[34]Department of Astrophysics, St. Petersburg State University, Universitetsky pr. 28, Petrodvoretz, 198504 St. Petersburg, Russia.
[35]Physics Department and McDonnell Center for the Space Sciences, Washington University in St. Louis, St. Louis, MO 63130, USA.

and on the first measurement of the linear polarization from an accreting neutron star. We also discuss how polarimetry can be used to constrain the basic geometry of the pulsar and test the hypothesis of free precession of the neutron star in this binary system, as well as the challenges it poses for X-ray pulsar emission models.

The source was observed by IXPE on 2022 February 17–24, at the beginning of the 35 d precession cycle, the so-called "main-on" state, as illustrated in Fig. 1. The observation started while the pulsar was still obscured by the outer edge of the warped and tilted accretion disc [10, 11] and continued throughout the first part of the main-on state where the neutron star emerges from behind the accretion disc and becomes visible directly [12]. IXPE had, therefore, a direct and clear view of the neutron star through most of the observation except for brief periods when the pulsar was eclipsed by the donor star, and the so-called "pre-eclipse" dips, associated with obscuration by the outer disc regions disturbed by the interaction with the accretion stream from the donor star [13] or by the gas stream itself [14]. The data taken during the eclipses of the pulsar and during periods of strong absorption were excluded from the analysis. This resulted in a total effective exposure time of 150 ks suitable for polarimetric and spectro-polarimetric analysis based on the formalism outlined by [15] and [16] and standard for all IXPE observations up to now, which is described in detail in Methods.

Results

We started the analysis by looking at the phase-averaged polarization of the emission from Her X-1, using all photons collected throughout the observation in the broad 2–7 keV energy band, ignoring the 7–8 keV band due a higher background and remaining calibration uncertainties. We detect a highly significant and well constrained polarization signal, with a polarization degree (PD) of 8.6 0.5% and polarization angle (PA, measured from north to east) of 62 2 (all uncertainties are quoted at 1 confidence level unless stated otherwise). The measured PD is significantly lower than the predicted 60–80% for the source [9], which opens the way for new theoretical investigations as we discuss below. We emphasise that the unexpectedly low polarization is clearly intrinsic to the radiation emerging from the pulsar, and cannot be explained with the signal being depolarized on its way from the pulsar to the observer, e.g., by scattering in the accretion flow or accretion disc atmosphere. Indeed, as already mentioned, the source is expected to be observed directly throughout most of the observation, and moreover, the PD appears to be minimal at the peak of the main-on where the flux is maximal and thus the amount of scattering material minimal as illustrated in Fig. 1. As the next step, we investigated the dependence of the polarization properties on photon energy. We find that both the PD and PA appear to be energy independent (see Fig. 2 and Extended Data Figure 1), with only an indication at 2 confidence level (see Methods) for the PD increasing towards higher energies. We continue,

233 **2.** Egonsson, J. & Hakala, P. Discovery of variable optical polarization in Her X-1. *Astron. Astrophys.*
234 **244**, L41–L42 (1991).

235 **3.** Truemper, J., Kahabka, P., Oegelman, H., Pietsch, W. & Voges, W. EXOSAT Observations of the
236 35 Day Cycle of Hercules X-1: Evidence for Neutron Star Precession. *Astrophys. J. Lett.* **300**, L63
237 (1986). DOI 10.1086/184604.

238 **4.** Staubert, R. *et al.* Two ~35 day clocks in Hercules X-1: evidence for neutron star free precession.
239 *Astron. Astrophys.* **494**, 1025–1030 (2009). DOI 10.1051/0004-6361:200810743. 0811.4045.

240 **5.** Postnov, K. *et al.* Variable neutron star free precession in Hercules X-1 from evolution of RXTE
241 X-ray pulse profiles with phase of the 35-d cycle. *Mon. Not. R. Astron. Soc.* **435**, 1147–1164 (2013).
242 DOI 10.1093/mnras/stt1363. 1307.6026.

243 **6.** Tananbaum, H. *et al.* Discovery of a Periodic Pulsating Binary X-Ray Source in Hercules from
244 UHURU. *Astrophys. J. Lett.* **174**, L143 (1972). DOI 10.1086/180968.

245 **7.** Bailer-Jones, C. A. L., Rybizki, J., Fouesneau, M., Demleitner, M. & Andrae, R. Estimating Distances
246 from Parallaxes. V. Geometric and Photogeometric Distances to 1.47 Billion Stars in Gaia Early Data
247 Release 3. *Astron. J.* **161**, 147 (2021). DOI 10.3847/1538-3881/abd806. 2012.05220.

248 **8.** Middleditch, J. & Nelson, J. Studies of optical pulsations from HZ Herculis/Hercules X-1: a
249 determination of the mass of the neutron star. *Astrophys. J.* **208**, 567–586 (1976). DOI 10.1086/154638.

250 **9.** Truemper, J. *et al.* Evidence for strong cyclotron line emission in the hard X-ray spectrum of Hercules
251 X-1. *Astrophys. J. Lett.* **219**, L105–L110 (1978). DOI 10.1086/182617.

252 **10.** Giacconi, R. *et al.* Further X-ray observations of Hercules X-1 from Uhuru. *Astrophys. J.* **184**, 227
253 (1973). DOI 10.1086/152321.

254 **11.** Leahy, D. A. Modelling the extreme ultraviolet emission during the low state of Hercules X-1. *Mon.*
255 *Not. R. Astron. Soc.* **342**, 446–452 (2003). DOI 10.1046/j.1365-8711.2003.06542.x.

256 **12.** Klochkov, D. K. *et al.* Observational manifestations of the change in the tilt of the accretion disk to
257 the orbital plane in her X-1/HZ her with phase of its 35-day period. *Astronomy Letters* **32**, 804–815
258 (2006). DOI 10.1134/S1063773706120024.

13. Leahy, D. & Wang, Y. The 35-Day Cycle of Hercules X-1 in Multiple Energy Bands from MAXI and Swift/BAT Monitoring. *Universe* **7**, 160 (2021). DOI 10.3390/universe7060160.

14. Igna, C. D. & Leahy, D. A. Light-curve dip production through accretion stream-accretion disc impact in the HZ Her/Her X-1 binary star system. *Mon. Not. R. Astron. Soc.* **425**, 8–20 (2012). DOI 10.1111/j.1365-2966.2012.21303.x.

15. Kislat, F., Beilicke, M., Guo, Q., Zajczyk, A. & Krawczynski, H. An unfolding method for X-ray spectro-polarimetry. *Astroparticle Physics* **64**, 40–48 (2015). DOI 10.1016/j.astropartphys.2014.11.003. 1411.5037.

16. Strohmayer, T. E. X-Ray Spectro-polarimetry with Photoelectric Polarimeters. *Astrophys. J.* **838**, 72 (2017). DOI 10.3847/1538-4357/aa643d. 1703.00949.

17. Gnedin, Y. N., Pavlov, G. G. & Shibanov, Y. A. The effect of vacuum birefringence in a magnetic field on the polarization and beaming of X-ray pulsars. *Soviet Astronomy Letters* **4**, 117–119 (1978).

18. Pavlov, G. G. & Shibanov, Y. A. Influence of vacuum polarization by a magnetic field on the propagation of electromagnetic waves in a plasma. *Soviet Journal Experimental Theoretical Physics* **49**, 741 (1979).

19. Heyl, J. S. & Shaviv, N. J. Polarization evolution in strong magnetic fields. *Mon. Not. R. Astron. Soc.* **311**, 555–564 (2000). DOI 10.1046/j.1365-8711.2000.03076.x. astro-ph/9909339.

20. Heyl, J. & Caiazzo, I. Strongly Magnetized Sources: QED and X-ray Polarization. *Galaxies* **6**, 76 (2018). DOI 10.3390/galaxies6030076. 1802.00358.

21. Blum, S. & Kraus, U. Analyzing X-Ray Pulsar Profiles: Geometry and Beam Pattern of Hercules X-1. *Astrophys. J.* **529**, 968–977 (2000). DOI 10.1086/308308. astro-ph/9909449.

22. Radhakrishnan, V. & Cooke, D. J. Magnetic Poles and the Polarization Structure of Pulsar Radiation. *Astrophys. Lett.* **3**, 225 (1969).

23. Biryukov, A. & Abolmasov, P. Magnetic angle evolution in accreting neutron stars. *Mon. Not. R. Astron. Soc.* **505**, 1775–1786 (2021). DOI 10.1093/mnras/stab1378. 2105.00754.

24. Caiazzo, I. & Heyl, J. Polarization of accreting X-ray pulsars. I. A new model. *Mon. Not. R. Astron. Soc.* **501**, 109–128 (2021). DOI 10.1093/mnras/staa3428. 2009.00631.

25. Weisskopf, M. C. *et al.* The Imaging X-Ray Polarimetry Explorer (IXPE): Pre-Launch. *J. Astron. Telesc. Instrum. Syst.* **8**, 026002 (2022). DOI 10.1117/1.JATIS.8.2.026002. 2112.01269.

26. Soffitta, P. *et al.* The Instrument of the Imaging X-Ray Polarimetry Explorer. *Astron. J.* **162**, 208 (2021). DOI 10.3847/1538-3881/ac19b0. 2108.00284.

27. Baldini, L. *et al.* Design, construction, and test of the Gas Pixel Detectors for the IXPE mission. *Astroparticle Physics* **133**, 102628 (2021). DOI 10.1016/j.astropartphys.2021.102628. 2107.05496.

28. Kislat, F., Clark, B., Beilicke, M. & Krawczynski, H. Analyzing the data from X-ray polarimeters with Stokes parameters. *Astroparticle Physics* **68**, 45–51 (2015). DOI 10.1016/j.astropartphys.2015.02.007. 1409.6214.

29. Baldini, L. *et al.* ixpeobssim: a Simulation and Analysis Framework for the Imaging X-ray Polarimetry Explorer. *arXiv e-prints* arXiv:2203.06384 (2022). 2203.06384.

30. Arnaud, K. A. XSPEC: The First Ten Years. In Jacoby, G. H. & Barnes, J. (eds.) *Astronomical Data Analysis Software and Systems V*, vol. 101 of *Astronomical Society of the Pacific Conference Series*, 17 (1996).

31. Rankin, J. *et al.* An Algorithm to Calibrate and Correct the Response to Unpolarized Radiation of the X-Ray Polarimeter Onboard IXPE. *Astron. J.* **163**, 39 (2022). DOI 10.3847/1538-3881/ac397f. 2111.14867.

32. Di Marco, A. *et al.* A Weighted Analysis to Improve the X-Ray Polarization Sensitivity of the Imaging X-ray Polarimetry Explorer. *Astron. J.* **163**, 170 (2022). DOI 10.3847/1538-3881/ac51c9. 2202.01093.

33. Życki, P. T., Done, C. & Smith, D. A. The 1989 May outburst of the soft X-ray transient GS 2023+338 (V404 Cyg). *Mon. Not. R. Astron. Soc.* **309**, 561–575 (1999). DOI 10.1046/j.1365-8711.1999.02885.x. astro-ph/9904304.

309 **34.** Wit, E., van den Heuvel, E. & Romeijn, J.-W. All models are wrong...': an introduction to model
310 uncertainty. *Statistica Neerlandica* **66**, 217–236 (2012). DOI 10.1111/j.1467-9574.2012.00530.x.

311 **35.** Staubert, R., Klochkov, D. & Wilms, J. Updating the orbital ephemeris of Hercules X-1; rate of
312 decay and eccentricity of the orbit. *Astron. Astrophys.* **500**, 883–889 (2009). DOI 10.1051/0004-
313 6361/200911690. 0904.2307.

314 **36.** Lomb, N. R. Least-Squares Frequency Analysis of Unequally Spaced Data. *Astrophys. Space Sci.* **39**,
315 447–462 (1976). DOI 10.1007/BF00648343.

316 **37.** Scargle, J. D. Studies in astronomical time series analysis. II. Statistical aspects of spectral analysis of
317 unevenly spaced data. *Astrophys. J.* **263**, 835–853 (1982). DOI 10.1086/160554.

318 **38.** Kuster, M. *et al.* Evolution of the 1.24s pulse profile during a Her X-1 turn-on. In Gimenez, A.,
319 Reglero, V. & Winkler, C. (eds.) *Exploring the Gamma-Ray Universe*, vol. 459 of *ESA Special*
320 *Publication*, 309–312 (2001).

321 **39.** Poutanen, J. Relativistic rotating vector model for X-ray millisecond pulsars. *Astron. Astrophys.* **641**,
322 A166 (2020). DOI 10.1051/0004-6361/202038689. 2006.10448.

323 **40.** Buchner, J. *et al.* X-ray spectral modelling of the AGN obscuring region in the CDFS: Bayesian model
324 selection and catalogue. *Astron. Astrophys.* **564**, A125 (2014). DOI 10.1051/0004-6361/201322971.
325 1402.0004.

326 **41.** Brown, J. C., McLean, I. S. & Emslie, A. G. Polarisation by Thomson scattering in optically thin
327 stellar envelopes. II. Binary and multiple star envelopes and the determination of binary inclinations.
328 *Astron. Astrophys.* **68**, 415–427 (1978).

329 **42.** Drissen, L., Lamontagne, R., Moffat, A. F. J., Bastien, P. & Seguin, M. Spectroscopic and Polarimetric
330 Parameters of the Runaway WN7 Binary System HD 197406: Is the Secondary an X-Ray–quiet Black
331 Hole? *Astrophys. J.* **304**, 188 (1986). DOI 10.1086/164153.

332 **43.** Kravtsov, V. *et al.* Orbital variability of the optical linear polarization of the γ-ray binary LS I
333 +61° 303 and new constraints on the orbital parameters. *Astron. Astrophys.* **643**, A170 (2020). DOI
334 10.1051/0004-6361/202038745. 2010.00999.

44. Reynolds, A. P. *et al.* A new mass estimate for Hercules X-1. *Mon. Not. R. Astron. Soc.* **288**, 43–52 (1997). DOI 10.1093/mnras/288.1.43.

45. Leahy, D. A. & Abdallah, M. H. HZ Her: Stellar Radius from X-Ray Eclipse Observations, Evolutionary State, and a New Distance. *Astrophys. J.* **793**, 79 (2014). DOI 10.1088/0004-637X/793/2/79. 1406.6138.

46. Wolff, M. T. *et al.* The NuSTAR X-Ray Spectrum of Hercules X-1: A Radiation-dominated Radiative Shock. *Astrophys. J.* **831**, 194 (2016). DOI 10.3847/0004-637X/831/2/194. 1608.08978.

47. Mushtukov, A. A., Suleimanov, V. F., Tsygankov, S. S. & Poutanen, J. The critical accretion luminosity for magnetized neutron stars. *Mon. Not. R. Astron. Soc.* **447**, 1847–1856 (2015). DOI 10.1093/mnras/stu2484. 1409.6457.

48. Staubert, R. *et al.* Discovery of a flux-related change of the cyclotron line energy in Hercules X-1. *Astron. Astrophys.* **465**, L25–L28 (2007). DOI 10.1051/0004-6361:20077098. astro-ph/0702490.

49. Zel'dovich, Y. B. & Shakura, N. I. X-Ray Emission Accompanying the Accretion of Gas by a Neutron Star. *Soviet Ast.* **13**, 175 (1969).

50. Suleimanov, V. F., Poutanen, J. & Werner, K. Accretion heated atmospheres of X-ray bursting neutron stars. *Astron. Astrophys.* **619**, A114 (2018). DOI 10.1051/0004-6361/201833581. 1808.10655.

51. González-Caniulef, D., Zane, S., Turolla, R. & Wu, K. Atmosphere of strongly magnetized neutron stars heated by particle bombardment. *Mon. Not. R. Astron. Soc.* **483**, 599–613 (2019). DOI 10.1093/mnras/sty3159. 1811.08526.

52. Mushtukov, A. A., Suleimanov, V. F., Tsygankov, S. S. & Portegies Zwart, S. Spectrum formation in X-ray pulsars at very low mass accretion rate: Monte Carlo approach. *Mon. Not. R. Astron. Soc.* **503**, 5193–5203 (2021). DOI 10.1093/mnras/stab811. 2006.13596.

53. van Adelsberg, M. & Lai, D. Atmosphere models of magnetized neutron stars: QED effects, radiation spectra and polarization signals. *Mon. Not. R. Astron. Soc.* **373**, 1495–1522 (2006). DOI 10.1111/j.1365-2966.2006.11098.x. astro-ph/0607168.

54. Suleimanov, V., Potekhin, A. Y. & Werner, K. Models of magnetized neutron star atmospheres: thin atmospheres and partially ionized hydrogen atmospheres with vacuum polarization. *Astron. Astrophys.* **500**, 891–899 (2009). DOI 10.1051/0004-6361/200912121. 0905.3276.

55. Pavlov, G. G. & Zavlin, V. E. Polarization of Thermal X-Rays from Isolated Neutron Stars. *Astrophys. J.* **529**, 1011–1018 (2000). DOI 10.1086/308313. astro-ph/9909326.

Acknowledgements

This paper is based on the observations made by the Imaging X-ray Polarimetry Explorer (IXPE), a joint US and Italian mission. This research used data products provided by the IXPE Team (MSFC, SSDC, INAF, and INFN) and distributed with additional software tools by the High-Energy Astrophysics Science Archive Research Center (HEASARC), at NASA Goddard Space Flight Center (GSFC). The US contribution is supported by the National Aeronautics and Space Administration (NASA) and led and managed by its Marshall Space Flight Center (MSFC), with industry partner Ball Aerospace (contract NNM15AA18C). The Italian contribution is supported by the Italian Space Agency (Agenzia Spaziale Italiana, ASI) through contract ASI-OHBI-2017-12-I.0, agreements ASI-INAF-2017-12-H0 and ASI-INFN-2017.13-H0, and its Space Science Data Center (SSDC), and by the Istituto Nazionale di Astrofisica (INAF) and the Istituto Nazionale di Fisica Nucleare (INFN) in Italy. The research at Boston University was supported in part by National Science Foundation grant AST-2108622. V.D. and V.F.S. acknowledge support from the German Academic Exchange Service (DAAD) travel grant 57525212. V.F.S. thanks the German Research Foundation (DFG) grant WE 1312/53-1. J.P. and S.S.T. thank the Russian Science Foundation grant 20-12-00364 and the Academy of Finland grants 333112, 349144, 349373, and 349906 for support. I.C. is a Sherman Fairchild Fellow at Caltech and thanks the Burke Institute at Caltech for supporting her research. A.A.M. acknowledges support from the Netherlands Organization for Scientific Research Veni Fellowship.

Author contributions statement

V.D. analyzed the data and wrote the draft of the manuscript. J.P. led the work of the IXPE Topical Working Group on Accreting Neutron Stars and contributed to modeling geometrical parameters, interpretation and

the text. S.S.T. produced an independent analysis of the data. V.F.S. led modeling of the polarization from heated atmospheres. A.D.M., F.L.M., F.M., and J.R. provided quick-look analysis of the data and energy scale correction calculation. I.C., J.H., A.A.M., S.Z., R.S. and A.S. contributed to interpretation of the results and writing of the text. M.B. and G.G.P. acted as internal referees of the paper and contributed to interpretation. Other members of the IXPE collaboration contributed to the design of the mission and its science case and planning of the observations. All authors provided input and comments on the manuscript.

Methods

Analysis of IXPE data

IXPE includes three co-aligned X-ray telescopes, each comprising an X-ray mirror assembly (NASA-furnished), and linear polarization-sensitive pixelated Gas Pixel Detectors (GPDs, ASI-furnished) to provide imaging polarimetry over a nominal 2–8 keV band. A complete description of the hardware and its performance is given in[25–27]. The GPDs are, in essence, pixelated proportional counters, which allow to recover the direction for each primary photo-electron ejected upon the interaction of an incident photon with the detector medium. This direction and the track length carry information about the direction of electromagnetic field oscillation associated with each individual photon, and thus could be used to recover polarization properties (i.e. the Stokes parameters) for an astrophysical source through analysis of the distribution of track directions for all photons from the source. The amplitude of variation of the track angles for a 100% polarized source is described by the energy-dependent modulation factor. The values and the energy dependence of the modulation factor were calibrated both on ground and continuously monitored in space, and they are taken into account when modeling the polarization as described below.

IXPE data telemetered to the ground stations in Malindi (primary) and in Singapore (secondary) are transmitted to the Mission Operations Center (MOC) at the Laboratory for Atmospheric and Space Physics (University of Colorado) and then to the Science Operations Center (SOC) at the NASA Marshall Space Flight Center. Using the software developed jointly by the NASA and the ASI, the SOC processes science and relevant engineering and ancillary data, to produce the data products that are archived at the High-Energy Astrophysics Science Archive Research Center (HEASARC) at the NASA Goddard Space Flight Center, for use by the international astrophysics community. IXPE data are distributed in a lower level format (L1), where relevant information about event tracks are reported, and also in a higher level format (L2), where several corrections have been applied and only the main properties of the reconstructed events are reported. In particular, in the L2 the photon energy is obtained after corrections for temperature and gain effects. Further corrections for the gain effects are applied using the data from the on-board calibration sources acquired during the observation. The imaging information in L2 is obtained from the L1 after correcting for dithering of the spacecraft pointing and orbital thermally-induced motion of the

boom that separates the optics from the detectors. The L2 data were then screened and processed using the current version of the HEASOFT software and calibration files.

The data reduction consists of the following main steps. The track images are first processed to separate the signal from electronic noise and then a custom algorithm is applied to derive the characteristics of the event, that are, the direction of the photoelectron emission, the energy, the arrival time and the direction of the incoming photon. The subsequent steps are to calibrate both the energy and the response to polarization, and to filter bad events and time intervals in which the source was occulted by the Earth or there were pointing inaccuracies, etc.

After initial processing, various selection criteria may be imposed for detected photons. Those can include the energy (to study energy dependence of the polarization properties), the arrival time, the pulse or the orbital phase, or position on the detector (to study spatial dependence of the polarization properties in extended sources or to discriminate between source and background photons for point sources). On the selected event ensemble, the last step is to normalize the measured response to polarization by the modulation factor.

Analysis of polarization is carried out with two different approaches. The first one, based on the unbinned formalism presented in[28], is implemented in the IXPE collaboration software suite IXPEBOSSIM[29]. The other method relies on the procedure presented in[16], and it is based on the generation of the Stokes spectra, which are then fitted with standard spectral-fitting software, like XSPEC[30]. The proper instrument response functions are provided by the IXPE Team as a part of the IXPE calibration database released on 2022 March 14 and available in the HEASARC Calibration Database[1] All values reported below are based on the spectro-polarimetric fits of the Stokes spectra unless stated otherwise. The uncertainties are estimated using a Markov chain Monte Carlo (`mcmc`) method for respective parameter from spectro-polarimetric fits.

Pulse-phase averaged analysis. As a first step, we investigated the time-averaged polarization from the pulsar. The Stokes parameters are obtained from the L1 data using the unbinned approach of[28] and the spurious modulation is removed following the approach of[31]. The Stokes parameters in the L2 data are distributed with weights obtained following the procedure from[32], which can be used to perform a

[1] https://heasarc.gsfc.nasa.gov/docs/heasarc/caldb/caldb_supported_missions.html

weighted analysis improving the sensitivity for faint sources. Considering the low background level and the high number of source counts in the case of Her X-1, we do not use the weighted approach for the final results reported. We performed, however, both weighted and unweighted analyses and found compatible results.

The source and background photons were extracted from a circular (radius of 1′.6) and annular (with inner and outer radii of 2′.5 and 5′, respectively) regions centered at the source. The extraction radii were chosen to select the source with a proper margin; the background was later removed by subtracting its Stokes parameters, re-scaled for the appropriate extraction area, from those of the source. The average values of the Stokes parameters, and corresponding polarization degree (PD) and polarization angle (PA), were then estimated in a single 2–7 keV energy band and in four sub-bins covering the same energy range. Note that we conservatively ignored energies in 7–8 keV energy range to avoid potential systematic effects associated with the remaining energy scale uncertainties (which can be expected to have largest effect around the energies where effective area drops abruptly, i.e. around 8 keV) and uncertainties in the alignment of the optical axis at this stage of the mission, which affects vignetting correction (which is again strongest at highest energies). We emphasize, however, that these effects mostly affect spectral analysis (i.e. the best-fit parameters of the spectral model), and the polarimetric results are not affected.

In addition to the binned analysis, we have also conducted spectro-polarimetric modeling of the same data-set. In particular, the Stokes spectra were extracted for each detector unit and modeled simultaneously using absorbed NTHCOMP model[33] for intensity spectra in combination with either POLCONST or POLPOW polarimetric models. The NTHCOMP model describes a Comptonized spectrum from seed photons of a characteristic temperature $T_{\rm bb,comp}$ (defining the low energy rollover) by electrons with temperature $T_{\rm e,comp}$ (defining the high energy rollover). Instead of the Thomson optical depth this model is parametrized by the power-law index $\Gamma_{\rm comp}$, because the Comptonization spectrum for non-relativistic electron temperatures is well described by a power law between the photon seed energies and the cutoff energy related to the electron temperature. This model is often used to describe the spectra of X-ray pulsars. The model normalization at 1 keV, $A_{\rm comp}$, and cross-normalization constants defining relative normalization of IXPE detector units two and three relative to the first one, $C_{\rm DU2}$ and $C_{\rm DU3}$, were also considered as free parameters.

We emphasize that NTHCOMP is a purely phenomenological model and physical interpretation of

the best-fit values is not trivial as the model is actually not designed to describe the spectra of X-ray pulsars. The spectrum of Her X-1 is known to be more complex than given by this model (e.g. there is a blackbody-like component with $kT \sim 0.1 - 0.3$ keV and a cyclotron absorption line), but within the IXPE band the spectrum is well described by this simplified model. In fact, the phase-averaged spectrum can even be approximated with a single power law, but this does not apply to all phase bins, hence our choice of the next simplest model. We verified, however, that the choice of the intensity continuum model does not significantly affect any of the polarimetric measurements (as is also justified by the agreement between the binned analysis and the spectro-polarimetric analysis results).

It is worth noting that at the time of the Her X-1 observation, the IXPE telescope axes were slightly offset with respect to the pointing direction, and that there were uncertainties in modeling of the boom motion during the observation. This caused an additional vignetting with an impact on the effective area calibration and then on the spectral analysis. However, this has no impact on the measured dependence of the polarization on energy because the polarization is estimated after normalization of the Stokes parameters U and Q to the source flux, which cancels out the systematics related to the effective area. This is also confirmed by the analysis presented in Fig.1 and Extended Data Figure 1 and Extended Data Table 1, where the results for both individual and combined detectors data are reported. We emphasize a good agreement between the individual detectors and the two independent modeling approaches.

The polarization properties appear to be only weakly dependent on energy, although there is an indication of increase of the PD with energy. Indeed, although there appears to be a systematic increase of the PD towards higher energies, and the value of Pearson correlation coefficient between PD and energy of ~ 0.86 suggests moderate degree of correlation, the values in individual bins, except the first one, are consistent with the average value, as illustrated in Fig. 2. An alternative approach to assess the significance for such energy dependence is to compare the results of the spectro-polarimetric fits for models when polarization is assumed constant to those where it is energy-dependent, which are summarized in Extended Data Table 1. As evident from the table, the model where constant polarization is assumed yields slightly worse fit statistics, but a lower Bayesian information criterion (BIC) score[34], which makes it statistically preferred. Similar conclusion can be drawn based on the estimated significance of the deviation of the power-law index, characterizing the PD dependence on energy $\mathrm{PD}(E) \propto E^{-\Gamma_{\mathrm{PD}}}$, from zero, which is

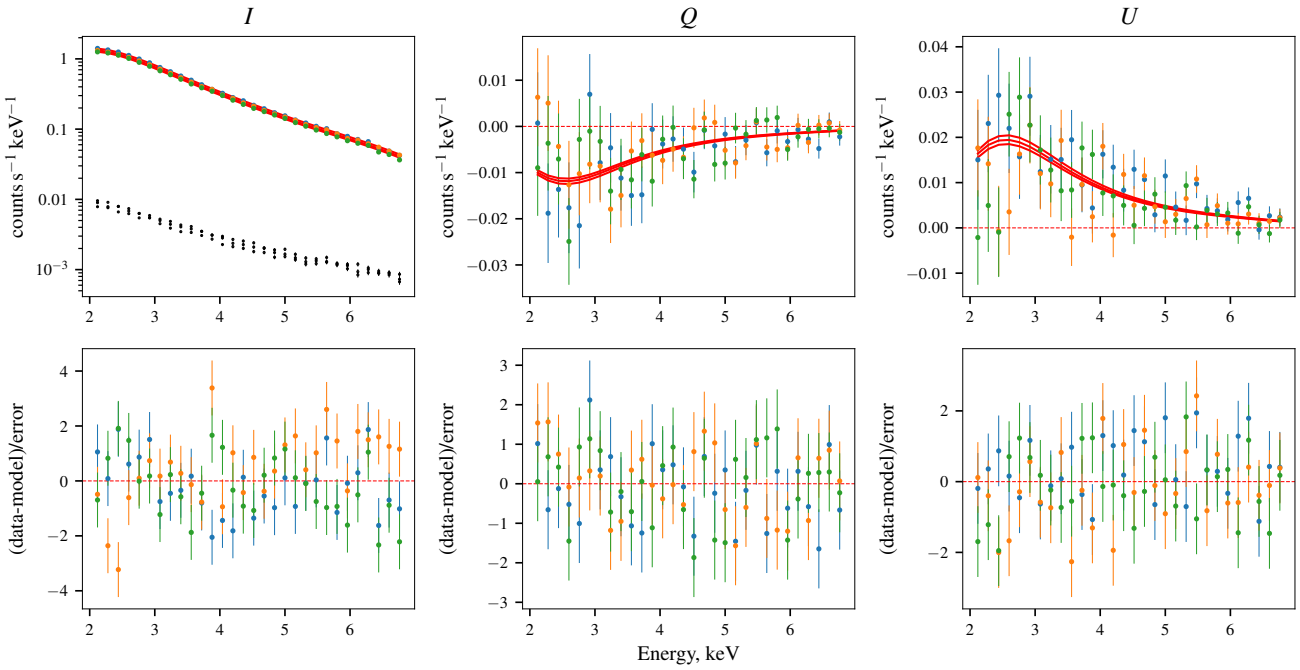

Extended Data Figure 1. Observed Stokes spectra of Her X-1. The top row shows spectra of the three Stokes parameters I, Q, and U, while the bottom row shows the residuals to the best-fit model (`nthcomp` for intensity and `polconst` for Q and U). The results for the three detector units are color-coded, the black points in the first panel show the estimated background level for each detector.

estimated at $\Gamma_{\rm PD} = -0.46 \pm 0.20$. It deviates from zero at the confidence level of only $\sim 98\%$, i.e. at $\sim 2\sigma$. The power-law index characterizing the dependence of the PA is estimated as $\Gamma_{\rm PA} = 0.04 \pm 0.10$, which is consistent with zero. We conclude, therefore, that there is no strong dependence of the polarization properties on energy, although there is an indication that the PD might actually increase with energy.

Pulse-phase and time-resolved analysis. In order to investigate the polarization properties as a function of the spin phase, we obtained a timing solution for the pulsar. As a first step, the arrival times of all events were corrected to the Solar system barycenter reference frame using the *barycorr* task, and then were corrected for effects of motion within binary system using ephemerides by[35]. After that, a Lomb-Scargle[36,37] periodogram was constructed to estimate the approximate value of the spin period and to obtain a template pulse profile which was used to estimate the residual phase delays and the pulse arrival times for observation segments by cross-correlation with the template (we considered continuous segments separated by at least 1 ks gaps as independent). The obtained pulse arrival times t_n were then used to obtain the final estimate of the spin period $p_{\rm spin} = 1.2377093(2)$ s using the phase connection

Extended Data Table 1. Average X-ray polarization of Her X-1. Pulse-phase averaged spectro-polarimetric fit results. The Stokes parameters spectra are modeled with `nthcomp` (I), and either constant polarization (`polconst`) model or model where a power-law type dependence is allowed for the PD and PA (`polpow`) for Q and U spectra. The uncertainties are reported at the 1σ confidence level based on `mcmc` chains obtained as described in the text.

Parameter	`polpow`	`polconst`
$\mathrm{PD}_{1\,\mathrm{keV}}$ (%)	$4.7^{+1.5}_{-1.2}$	8.6 ± 0.5
Γ_{PD}	-0.46 ± 0.20	
$\mathrm{PA}_{1\,\mathrm{keV}}$, deg	64^{+10}_{-9}	$60.2^{+1.8}_{-1.7}$
Γ_{PA}	0.04 ± 0.10	
$kT_{\mathrm{e,comp}}$, keV	$6.6^{+2.5}_{-1.4}$	$7.4^{+3.5}_{-2.0}$
$kT_{\mathrm{bb,comp}}$, keV	$0.349^{+0.015}_{-0.018}$	$0.345^{+0.017}_{-0.024}$
Γ_{comp}	$1.28^{+0.035}_{-0.05}$	$1.26^{+0.05}_{-0.06}$
A_{comp}	$0.0984^{+0.0033}_{-0.0027}$	$0.0990^{+0.004}_{-0.0028}$
C_{DU2}	0.9767 ± 0.0026	$0.9766^{+0.0026}_{-0.0025}$
C_{DU3}	$0.8923^{+0.0024}_{-0.0025}$	0.8922 ± 0.0024
χ^2/d.o.f./BIC	593.4/539/656.5	598.2/541/648.7

technique. In particular, we found that the observed arrival times were fully consistent with a constant period, i.e. $t_n = t_0 + n \times p_{\mathrm{spin}}$ as illustrated in Extended Data Figure 2. It is important to emphasize that no appreciable evolution of the pulse profile shape occurs during the observation as illustrated in Extended Data Figure 2 and expected on the basis of previous observations of the source at a similar phase of the precession cycle[38]. This allows us to use all the available data and achieve a sufficient sensitivity also in the individual phase bins. The observed pulsed fraction in the 2–7 keV band, defined through the maximum and minimum fluxes as $f = (F_{\mathrm{max}} - F_{\mathrm{min}})/(F_{\mathrm{max}} + F_{\mathrm{min}})$, is $\sim 55\%$.

Based on the available counting statistics and known instrument sensitivity, seven phase bins were then defined as shown in Fig. 3. The Stokes spectra ($I/Q/U$), and binned polarization cubes, were then extracted individually for each of the phase bins using IXPEOBSSIM package[29]. The background was assumed to be constant for all bins (which is justified since minor variations of the background rate during the observations are averaged out when folded with the spin period of the source). We used, therefore, Stokes spectra extracted for the entire observation as a background estimate in the phase-resolved analysis (after accounting for difference in the exposure). The extracted spectra were then modeled with the same model as the pulse-phase averaged spectra to derive the PD and PA using the `polconst` model. The final

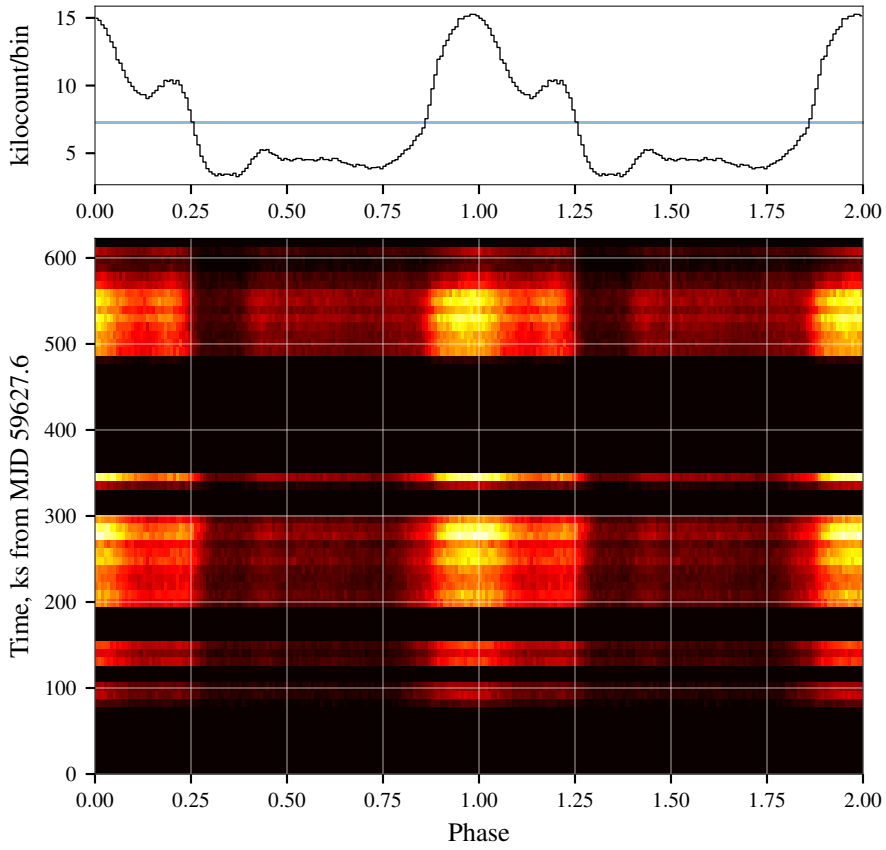

Extended Data Figure 2. Variation of the pulse profile of Her X-1 over the observation. Top panel shows the observed pulse profile averaged over entire observation (128 phase bins). The bottom panel shows the phaseogram, i.e. color-coded pulse profiles of individual observational segments folded with the same period, for the final timing solution obtained as discussed in the text. The phaseogram illustrates the lack of appreciable phase shifts (i.e. accuracy of the timing solution) and stability of the pulse profile shape during the observation.

Extended Data Table 2. Pulse-phase resolved X-ray polarization of Her X-1. Pulse-phase resolved spectro-polarimetric fit results for the `nthcomp` continuum flux and constant polarization `polconst` models. Uncertainties are reported at 1σ confidence level based on `mcmc` chains obtained as described in the text.

Phase	PD, %	PA, deg	$\Gamma_{\rm comp}$	$A_{\rm comp}/10^{-2}$	χ^2/d.o.f.
0.00–0.14	12.4 ± 1.9	46 ± 4	1.259 ± 0.007	4.56 ± 0.05	560.8/543
0.14–0.29	9.0 ± 1.7	50 ± 5	1.263 ± 0.006	5.88 ± 0.06	580.6/543
0.29–0.43	14.0 ± 1.8	47 ± 4	1.329 ± 0.008	5.96 ± 0.07	552.7/543
0.43–0.57	15.5 ± 1.7	56 ± 3	1.268 ± 0.006	5.83 ± 0.06	563.0/543
0.57–0.71	7.1 ± 1.0	78 ± 4	1.272 ± 0.004	16.06 ± 0.10	600.6/543
0.71–0.86	10.7 ± 1.1	71 ± 3	1.344 ± 0.004	17.44 ± 0.11	617.2/543
0.86–1.00	5.5 ± 1.2	48 ± 6	1.286 ± 0.004	11.99 ± 0.08	676.5/543

values and uncertainties were estimated based on *mcmc* chains produced using the `chain` command in XSPEC and are reported in Extended Data Table 2. We verified the consistency of the spectro-polarimetric and binned analysis results for all bins and found no significant differences in the phase dependence of the PD and PA, therefore only the results of the spectro-polarimetric analysis are reported.

The same procedure has been used to investigate the time dependence of the polarization properties over the observation. The full dataset was split into seven intervals separated by large gaps defined either by the instrumental good time intervals or by the eclipses of the source. For each interval, the Stokes spectra $(I/Q/U)$ were extracted and jointly modeled using `nthcomp` and `polconst` models to estimate the PD and PA values. The value of the power-law index in `nthcomp` model was considered as a free parameter to accommodate possible minor changes in the spectral shape over the observation. The final values and uncertainties were estimated based on *mcmc* chains produced using `chain` command in XSPEC and are reported in Extended Data Table 3. Again, we verified consistency of the spectro-polarimetric and the binned analysis results for all bins and found no significant differences in the phase dependence of the PD and PA, therefore again only results of the spectro-polarimetric analysis are reported.

Extended Data Table 3. Evolution of X-ray polarization of Her X-1. Time-resolved spin-phase averaged spectro-polarimetric fit results for `nthcomp` continuum flux and constant polarization `polconst` models. Uncertainties are reported at the 1σ confidence level based on the `mcmc` chains obtained as described in the text.

Time interval, MJD	PD,%	PA, deg	$\Gamma_{\rm comp}$	$A_{\rm comp}$	χ^2/dof
59628.53–59628.84	14.2 ± 2.4	66 ± 5	1.113 ± 0.003	0.0313 ± 0.0004	606.3/543
59629.07–59629.39	11.9 ± 1.8	66 ± 4	1.249 ± 0.006	0.0716 ± 0.0008	529.6/543
59629.86–59630.47	7.0 ± 1.2	61 ± 5	1.281 ± 0.004	0.0982 ± 0.0007	525.9/543
59630.45–59631.06	6.9 ± 1.0	60 ± 4	1.282 ± 0.004	0.1101 ± 0.0007	607.2/543
59631.49–59631.66	7.7 ± 2.0	54 ± 7	1.288 ± 0.007	0.1187 ± 0.0013	577.5/543
59633.19–59633.82	9.8 ± 1.1	59 ± 3	1.351 ± 0.005	0.1169 ± 0.0008	588.1/543
59633.75–59634.33	9.3 ± 1.2	58 ± 4	1.337 ± 0.005	0.1066 ± 0.0007	571.8/543

Geometry

X-ray polarimetry. Linearly polarized radiation observed from a spot at a neutron star can be described in the main polarization basis related to the projection of the angular momentum onto the plane of the sky:

$$\hat{\mathbf{e}}_1^{\rm m} = \frac{\hat{\Omega}_{\rm p} - \cos i_{\rm p}\,\hat{\mathbf{o}}}{\sin i_{\rm p}} = (-\cos i_{\rm p}, 0, \sin i_{\rm p}), \quad (1)$$

$$\hat{\mathbf{e}}_2^{\rm m} = \frac{\hat{\mathbf{o}}\times\hat{\Omega}_{\rm p}}{\sin i_{\rm p}} = (0,-1,0), \quad (2)$$

where $\hat{\Omega}_{\rm p} = (0,0,1)$ denotes the unit vector along the pulsar angular momentum, $\hat{\mathbf{o}} = (\sin i_{\rm p}, 0, \cos i_{\rm p})$ gives direction to the observer, and $i_{\rm p}$ is the inclination of the neutron star angular momentum to the line of sight (defined in the interval $[0^\circ, 180^\circ]$): $\cos i_{\rm p} = \hat{\mathbf{o}}\cdot\hat{\Omega}_{\rm p}$ (see Fig. 4).

If magnetic dipole vector is inclined to the spin axis by the angle θ (the magnetic obliquity), then it changes with the pulsar phase ϕ as $\hat{\mathbf{d}} = (\sin\theta\cos\phi, \sin\theta\sin\phi, \cos\theta)$. The angle ψ between the dipole and the line of sight is given by

$$\cos\psi \equiv \hat{\mathbf{o}}\cdot\hat{\mathbf{d}} = \cos i_{\rm p}\ \cos\theta + \sin i_{\rm p}\ \sin\theta\ \cos\phi. \quad (3)$$

If the pulsar radiation is dominated by the ordinary O-mode, the polarization vector lies in the plane formed by the vector of the dipole $\hat{\mathbf{d}}$ and the direction to the observer $\hat{\mathbf{o}}$. The corresponding polarization

basis that describes radiation escaping from the neutron star surface is

$$\hat{\mathbf{e}}_1^{\rm s} = \frac{\hat{\mathbf{d}} - \cos\psi\,\hat{\mathbf{o}}}{\sin\psi}, \quad \hat{\mathbf{e}}_2^{\rm s} = \frac{\hat{\mathbf{o}}\times\hat{\mathbf{d}}}{\sin\psi}. \tag{4}$$

The PA χ_0 measured from the projection of the spin axis onto the plane of the sky in the counter-clockwise direction is given by:

$$\cos\chi_0 = \hat{\mathbf{e}}_1^{\rm m}\cdot\hat{\mathbf{e}}_1^{\rm s} = \hat{\mathbf{e}}_2^{\rm m}\cdot\hat{\mathbf{e}}_2^{\rm s} = \frac{\sin i_{\rm p}\,\cos\theta - \cos i_{\rm p}\,\sin\theta\,\cos\phi}{\sin\psi}, \tag{5}$$

$$\sin\chi_0 = \hat{\mathbf{e}}_2^{\rm m}\cdot\hat{\mathbf{e}}_1^{\rm s} = -\hat{\mathbf{e}}_1^{\rm m}\cdot\hat{\mathbf{e}}_2^{\rm s} = -\frac{\sin\theta\,\sin\phi}{\sin\psi}. \tag{6}$$

We thus get the expression for the PA as in the rotating vector model (RVM)[22,39]

$$\tan\chi_0 = \frac{-\sin\theta\,\sin\phi}{\sin i_{\rm p}\,\cos\theta - \cos i_{\rm p}\,\sin\theta\,\cos\phi}. \tag{7}$$

If the position angle (measured from north to east) of the pulsar angular momentum is $\chi_{\rm p}$, then PA=$\chi_{\rm p}+\chi_0$. Thus variations of the X-ray PA with the pulsar phase ϕ can be fitted with the expression

$$\tan({\rm PA}-\chi_{\rm p}) = \frac{-\sin\theta\,\sin(\phi-\phi_0)}{\sin i_{\rm p}\,\cos\theta - \cos i_{\rm p}\,\sin\theta\,\cos(\phi-\phi_0)}, \tag{8}$$

where ϕ_0 is the phase of the light curve when the spot is closest to the observer.

Using Bayesian inference code BXA[40], we fit the PA data from Extended Data Table 2 with that model with four free parameters ($\chi_{\rm p}$, θ, $i_{\rm p}$, and ϕ_0). We assume flat priors for all parameters: $\chi_{\rm p}\in[-90^\circ,90^\circ]$, $\theta\in[0^\circ,90^\circ]$, $i_{\rm p}\in[0^\circ,180^\circ]$, and $\phi_0/(2\pi)\in[-0.5,0.5]$. The resulting posterior distributions are shown in Extended Data Figure 3. The magnetic obliquity and the pulsar position angle are both well constrained $\theta = 12.^\circ1\pm3.^\circ7$ and $\chi_{\rm p}=\chi_{\rm p,*}=56.^\circ9\pm1.^\circ6$, while the pulsar inclination has a rather large uncertainty, $i_{\rm p}=95^\circ\pm37^\circ$, with the posterior probability distribution extending from 0° all the way up to 180°, that

can be fitted by the function

$$\frac{dp}{di_{\rm p}} \propto \begin{cases} \sin^{1.5}(90^\circ\ i_{\rm p}/i_{\rm peak}), & i_{\rm p} \le i_{\rm peak} \\ \sin^{1.4}[90^\circ\ (2i_{\rm peak} - i_{\rm p} - 180^\circ)/(i_{\rm peak} - 180^\circ)], & i_{\rm p} > i_{\rm peak}, \end{cases} \tag{9}$$

where $i_{\rm peak} = 97^\circ$ is the angle where the distribution peaks. Because polarization cannot distinguish between oppositely directed pulsar spins, there is another solution $\chi_{\rm p} = \chi_{\rm p,*} \pm 180^\circ$. If radiation escaping from the pulsar is polarized perpendicular to the magnetic field direction (i.e. in the X-mode), then the position angle of the pulsar spin can have two possible values: $\chi_{\rm p} = \chi_{\rm p,*} \pm 90^\circ = 146.^\circ9 \pm 1.^\circ6$ or $-33.^\circ1 \pm 1.^\circ6$. Other angles are not affected by the spin direction.

Optical polarimetry. Orbital variation of the optical polarization was detected from Her X-1 by[2]. We fitted the phase curves of the normalized Stokes parameters digitalized from their Fig. 1 with the Fourier series

$$\begin{aligned} q &= q_0 + q_1\cos\varphi + q_2\sin\varphi + q_3\cos 2\varphi + q_4\sin 2\varphi, \\ u &= u_0 + u_1\cos\varphi + u_2\sin\varphi + u_3\cos 2\varphi + u_4\sin 2\varphi, \end{aligned} \tag{10}$$

where φ is the orbital phase. If the polarization is produced by Thomson scattering in an optically thin medium co-rotating with the system, the orbital orientation can be obtained from the Fourier coefficients[41]. The best-fit Fourier coefficients and their errors obtained by us are given in Extended Data Table 4 and are close to those reported in[2]. These coefficients can be used to derive the inclination $i_{\rm orb}$ of the binary orbit and the position angle $\chi_{\rm orb}$ of the projection of the orbital axis[42,43]:

$$\left(\frac{1-\cos i_{\rm orb}}{1+\cos i_{\rm orb}}\right)^4 = \frac{(u_3+q_4)^2 + (u_4-q_3)^2}{(u_4+q_3)^2 + (u_3-q_4)^2}, \tag{11}$$

$$\tan(2\chi_{\rm orb}) = \frac{A+B}{C+D}, \tag{12}$$

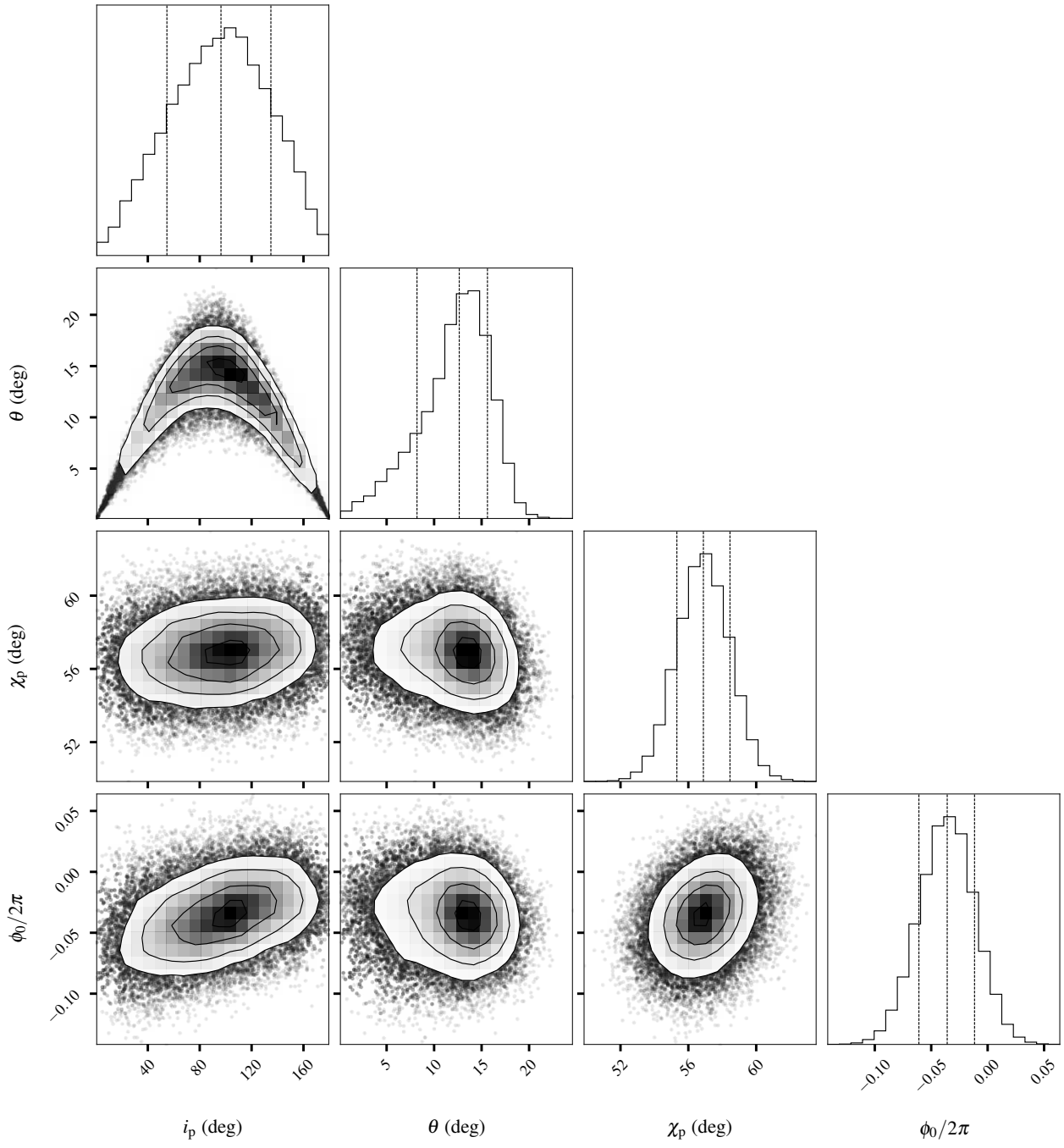

Extended Data Figure 3. Posterior distribution corner plot for the RVM fit of the PA phase dependence. The contours correspond to two-dimensional 1, 2, and 3σ levels.

Extended Data Table 4. Optical polarization of Her X-1. Fourier coefficients and their errors obtained by re-fitting the optical polarimetric data from ref.[2] with Eq. (10).

Stokes	q_0/u_0	q_1/u_1	q_2/u_2	q_3/u_3	q_4/u_4	χ^2/dof
q	0.015 ± 0.012	0.005 ± 0.012	0.002 ± 0.020	-0.080 ± 0.018	-0.034 ± 0.018	17.0/11
u	0.102 ± 0.016	0.006 ± 0.016	0.035 ± 0.026	-0.118 ± 0.024	0.040 ± 0.023	12.7/11

where

$$\begin{aligned} A &= \frac{u_4 - q_3}{(1-\cos i_{\rm orb})^2}, \quad B = \frac{u_4 + q_3}{(1+\cos i_{\rm orb})^2}, \\ C &= \frac{q_4 - u_3}{(1+\cos i_{\rm orb})^2}, \quad D = \frac{u_3 + q_4}{(1-\cos i_{\rm orb})^2}. \end{aligned} \tag{13}$$

These formulae give us $i_{\rm orb} = 100.^\circ4 \pm 4.^\circ9$ and $\chi_{\rm orb} = \chi_{\rm orb,*} = 28.^\circ9 \pm 5.^\circ9$ (or $\chi_{\rm orb} = \chi_{\rm orb,*} - 180^\circ = -151.^\circ1 \pm 5.^\circ9$ which is equally acceptable since only the orientation of the polarization plane can be measured). We note here that the orbital inclination is larger than 90°, which might appear to be at odds with the literature estimates for orbital inclination $i_{\rm orb} \sim 80^\circ - 90^\circ$[44,45].

We note, however, that these estimates are based on modeling of the donor star radius from optical spectroscopy and X-ray eclipses, and cannot distinguish between clockwise and counter-clockwise rotation (i.e. between inclinations $i_{\rm orb} < 90^\circ$ and $180^\circ - i_{\rm orb}$). In particular, the estimates listed in Table 8 of[45] seem to favor inclinations in the range $i_{\rm orb} \sim 80^\circ - 83^\circ$ or $180^\circ - i_{\rm orb} \sim 97^\circ - 100^\circ$ for the distance range of 6.5–7.5 kpc, estimated from Gaia EDR3 data[7]. This implies that our estimate is fully consistent with the literature values, and that the binary is rotating clockwise on the sky. We emphasize that this is a new result which can only be obtained from polarimetry, in this case, in the optical band.

Misalignment between pulsar and orbital spins. Using constraints on the 3D orientation of the pulsar and the orbit, we now can obtain the misalignment angle β between the pulsar and the orbital angular momenta:

$$\cos\beta = \cos i_{\rm p} \cos i_{\rm orb} + \sin i_{\rm p} \sin i_{\rm orb} \cos\Delta, \tag{14}$$

where $\Delta = \chi_{\rm p} - \chi_{\rm orb}$ is the difference between the position angles of the pulsar spin vector and the orbital angular momentum (the geometry is illustrated in Fig. 4). The parameters we use are given in Extended

Extended Data Table 5. Orbital and pulsar geometrical parameters of Her X-1.

$\chi_{\rm p,*}$ deg	θ deg	$i_{\rm p}$ deg	$\chi_{\rm orb,*}$ deg	$i_{\rm orb}$ deg
56.9 ± 1.6	12.1 ± 3.7	Eq. (9)	28.9 ± 5.9	100.4 ± 4.9

Extended Data Table 6. Misalignment angle. Misalignment angle β between the pulsar and orbital spins is computed for the four possible cases identified by letters A–D of the pulsar spin orientation. Here we assume $\chi_{\rm orb} = \chi_{\rm orb,*}$. The errors correspond to the 68% confidence level. The probability distributions for the cases A–D are shown in Extended Data Figure 4. If the orbital spin position angle differs by 180° from $\chi_{\rm orb,*}$, the resulting constraints on β are the same if $\chi_{\rm p}$ is also rotated by 180°.

	O-mode polarization		X-mode polarization	
Case	A	B	C	D
$\chi_{\rm p}$ (deg)	$\chi_{\rm p,*} = 56.9 \pm 1.6$	$\chi_{\rm p,*} \pm 180°$	$\chi_{\rm p,*} + 90°$	$\chi_{\rm p,*} - 90°$
β (deg)	33^{+18}_{-9}	147^{+9}_{-20}	115^{+8}_{-10}	63^{+10}_{-7}

Data Table 5. Assuming normal distributions for $\chi_{\rm p}$ and $\chi_{\rm orb}$ with the corresponding 1σ errors obtained above, a normal distribution for $i_{\rm orb}$ from the optical polarimetry, and the posterior distribution for $i_{\rm p}$ given by Equation (9), we make Monte-Carlo simulations to obtain a probability distribution for β, which is shown in Extended Data Figure 4 (see also Extended Data Table 6). For radiation in the O-mode (when $\chi_{\rm p} = \chi_{\rm p,*} = 56.^{\circ}9 \pm 1.^{\circ}6$ and taking $\chi_{\rm orb} = 28.^{\circ}9 \pm 5.^{\circ}9$), we get the smallest misalignment β with the distribution peaking at $\sim 30°$ and the lower limit being $\sim 20°$ at the 90% confidence level (see Extended Data Figure 4A). If $\chi_{\rm p} = \chi_{\rm p,*} \pm 180°$ (or $\chi_{\rm orb} = \chi_{\rm orb,*} \pm 180°$), the misalignment is much larger, with β peaking at 145° (Extended Data Figure 4B). For the X-mode polarization, $\chi_{\rm p} = \chi_{\rm p,*} \pm 90°$, β peaks at $\sim 115°$ or $\sim 65°$ (Extended Data Figure 4C,D). These results are practically unaffected by the exact form of the distribution of $i_{\rm p}$.

Modeling polarization from heated neutron star atmosphere

Polarization from a strongly magnetized accreting neutron star is largely defined by the emission region structure which is not known. Earlier estimates for Her X-1[1] were based on the accretion column model[46] which seems to be consistent with the observed broadband spectrum. The observed polarization, however, is significantly lower ($\sim$5–15%) than the predicted one (60–80%), requiring modifications to the models. There are several mechanisms that may depolarize radiation as it leaves the accretion column and travels through the magnetosphere. For instance, the depolarization can be caused by passing of radiation from

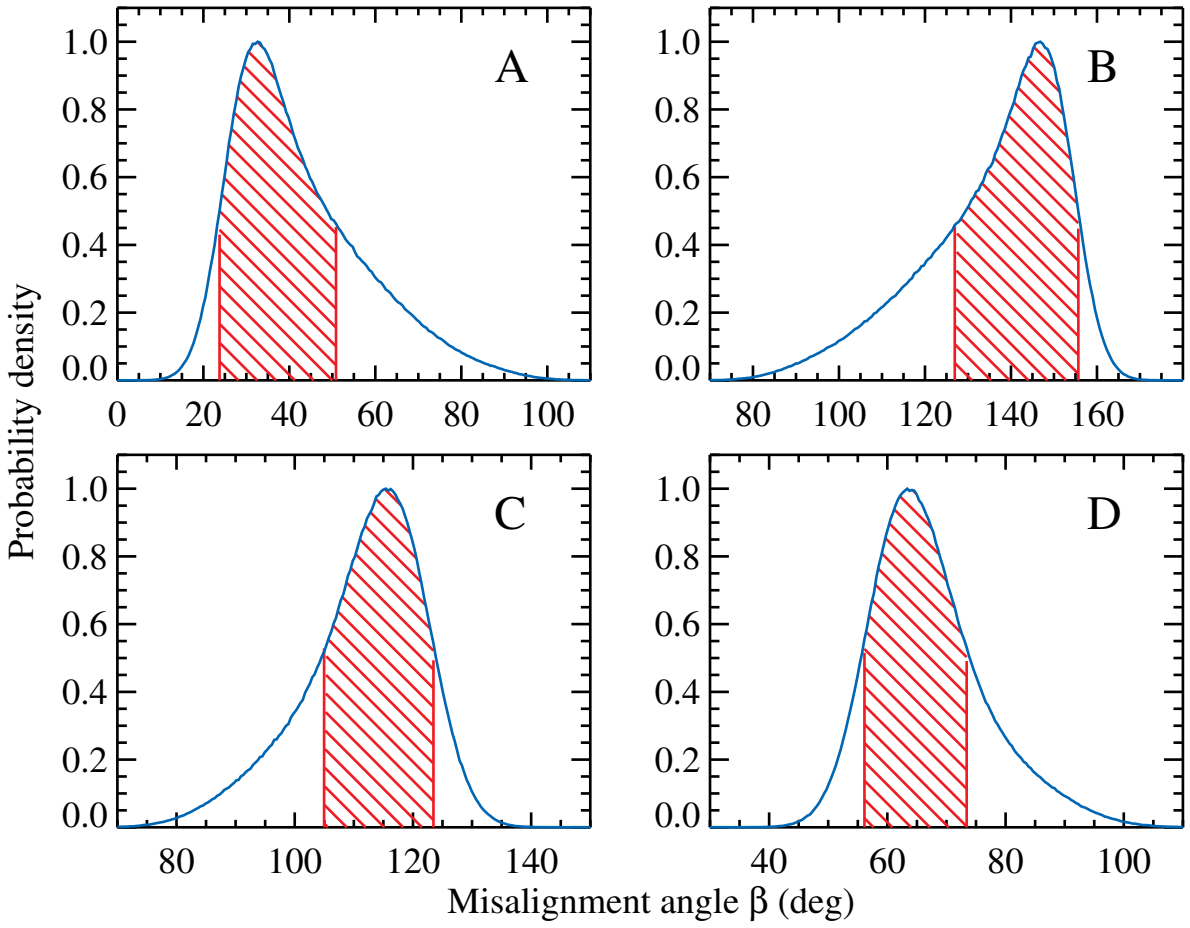

Extended Data Figure 4. Probability distribution function for the misalignment angle. The distribution normalized to the peak value is shown for the misalignment angle between the pulsar and the orbital angular momenta. The red hatched region corresponds to the 68% confidence interval (i.e. between 16th and 84th percentiles of the posterior probability distribution). Four panels correspond to four different cases for the choice of $\chi_{\rm p}$: **(A)** $\chi_{\rm p} = \chi_{\rm p,*} = 56.^{\circ}9 \pm 1.^{\circ}6$; **(B)** $\chi_{\rm p} = \chi_{\rm p,*} + 180^{\circ}$; **(C)** $\chi_{\rm p} = \chi_{\rm p,*} + 90^{\circ}$; **(D)** $\chi_{\rm p} = \chi_{\rm p,*} - 90^{\circ}$. Here we take $\chi_{\rm orb} = \chi_{\rm orb,*} = 28.^{\circ}9 \pm 5.^{\circ}9$.

the accretion column through the so-called vacuum resonance, where the contributions of plasma and magnetized vacuum to the dielectric tensor cancel each other and fast transformation of the normal modes of radiation occurs[17,18]. If the place where the final scattering of radiation takes place (i.e. the photosphere) also lies in this region, we expect substantial Faraday depolarization reducing the PD without changing the spectral energy distribution or the pulse profile. Furthermore, as the radiation travels from the column through the magnetosphere, generally it will pass through a region where the direction of propagation is nearly parallel to the magnetic field lines. Depending on the geometry of the emission region and the photon energy this can also result in substantial depolarization[24].

On the other hand, it is unclear whether an accretion column is present at all in Her X-1. Although the observed luminosity is close to the critical value[47], the source demonstrates a positive correlation of the cyclotron line energy with luminosity[48], which implies that the accreting pulsar is in a sub-critical state, when the energy of the infalling matter is dissipated at the neutron star surface but not in a radiation-dominated shock above it. In such a situation, fast ions of the accretion flow heat the neutron star atmosphere, and the thermal photons emerging from this heated atmosphere back-scatter on the in-falling electrons of the accretion flow with a corresponding energy gain (bulk Comptonization), and these back-scattered photons additionally heat the upper atmosphere. If the local mass accretion rate is close to the critical one, almost all the emergent photons will be back-scattered, and, as a result, radiation escapes primarily along the tangential direction to the neutron star surface, forming a "fan"-like angular distribution of the escaping radiation helping to explain the observed high pulsed fraction. An accurate self-consistent numerical model describing the processes above is yet to be developed. Here we consider a toy model of the overheated magnetized model atmosphere to demonstrate how the observed low polarization can be produced. Such models have been used for interpretation of accreting neutron stars[49–52] although it is important to emphasize that the broadband spectrum of Her X-1 is clearly not described by any of these models alone.

In this simplified picture, the key process that is responsible for low polarization is a mode conversion at the vacuum resonance. For a given photon energy and magnetic field strength, the vacuum resonance occurs at a plasma density of $\rho_{\rm V} \approx 10^{-4}(B/10^{12}\ {\rm G})^2 E_{\rm keV}^2\ {\rm g\,cm^{-3}}$[18]. At that density, the contribution of the virtual electron-positron pairs to the dielectric tensor becomes equal to the plasma contribution, and

618 the ordinary (O) and extraordinary (X) modes of radiation can convert to each other. Here we consider
619 the radiation transfer in magnetized plasma in the approximation of these two modes instead of the full
620 description in terms of Stokes parameters. We found that the modes become close to each other at a given
621 photon energy in the emergent spectrum if the vacuum resonance is located in the transition atmospheric
622 layer with a strong temperature gradient from the upper overheated layer of a temperature a few tens of
623 keVs to the lower layer of the atmosphere where the temperature is about 1–2 keV.

We illustrate this statement with a toy model of the transition region between two atmospheric parts (see Extended Data Figure 5A). We assume the surface magnetic field strength $B = 4 \times 10^{12}$ G, the temperature of the overheated layers $T_{\rm up} = 3.1 \times 10^8$ K, and the temperature of the bottom cold atmosphere $T_{\rm low} = 1.5 \times 10^7$ K. We consider three different transition depths of $m_{\rm up} = 0.3$, 3, and 30 g cm^{-2}. The corresponding gas pressure is determined by the product of the column density of plasma m and the surface gravity g, $P_{\rm gas} = gm$, computed using the neutron star mass $M = 1.4 M_\odot$ and radius $R = 12$ km. For the temperature structure we adopt the dependence

$$T(m) = \frac{T_{\rm up} - T_{\rm low}}{\exp[6(m/m_{\rm up} - 1)] + 1} + T_{\rm low}. \tag{15}$$

624 We solved the radiation transfer equation for the two modes using the magnetic opacities and the
625 mode conversion as described in[53], with no external radiation flux as the upper boundary condition and
626 the Planck function for the intensity as the lower boundary condition[54]. The polarization fraction of the
627 emergent flux in the observed energy band with and without mode conversion is shown in Extended
628 Data Figure 5B. The model with the transition depth $m_{\rm up} = 3$ g cm^{-2} demonstrates a low polarization,
629 which is explained by the mode conversion at the transition region with the strong temperature gradient,
630 see Extended Data Figure 6. We note that models with either thinner or thicker overheated layers yield
631 a higher polarization degree (i.e. a larger fraction of total flux is in one of the modes); however, the
632 dominant modes are different in these cases (Extended Data Figure 5B). If the thickness of the upper
633 layer is low, $m_{\rm up}$= 0.3 g cm^{-2}, the vacuum resonance occurs in the cold inner part of the atmosphere with
634 strong mode conversion. As a result, the O-mode dominates. On the other hand, the mode conversion
635 is inefficient if the vacuum resonance occurs within the overheated layer with $m_{\rm up}$= 30 g cm^{-2}, so the

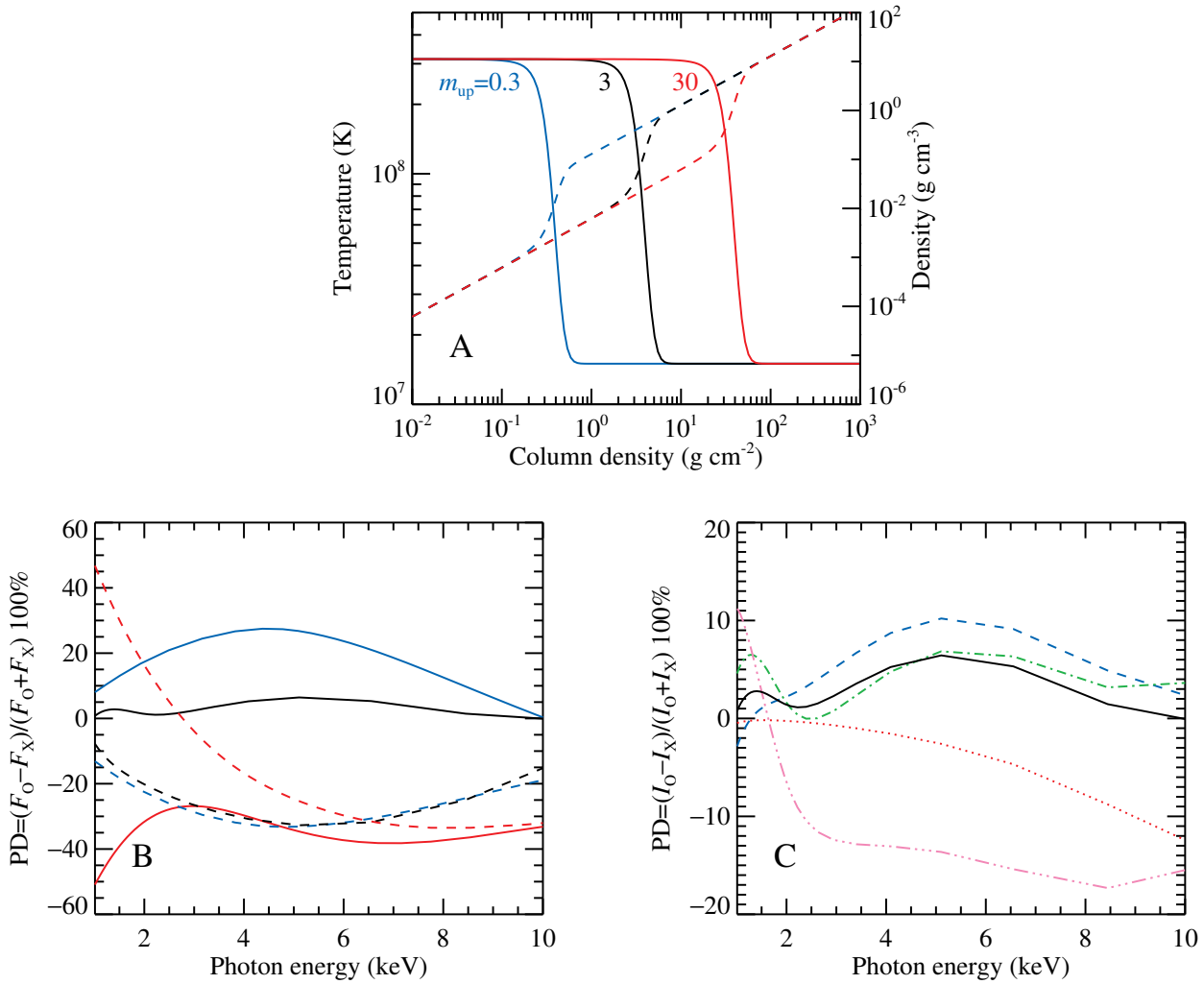

Extended Data Figure 5. Structure of the heated layer and the emergent polarization. (A) Temperature dependencies on column density (solid curves, left axis) and the corresponding density dependencies (dashed curves, right axis) for three different mass column densities of the heated layer $m_{\rm up} = 0.3, 3$, and 30 g cm^{-2} are shown with blue, black and red colors. **(B)** PD of the emergent angle-integrated flux as a function of the photon energy in the IXPE energy band for the three models with the mode conversion taken into account (solid curves) and without the mode conversion (dashed curves). **(C)** PD of the emergent radiation intensity as a function of the photon energy for the model $m_{\rm up} = 3$ g cm^{-2} with the mode conversion taken into account. Colored lines correspond to the zenith angles of 10° (red dotted), 30° (blue dashed), 60° (green dot-dashed), and 81° (pink triple-dot-dashed), while the black solid line corresponds to the PD of the flux.

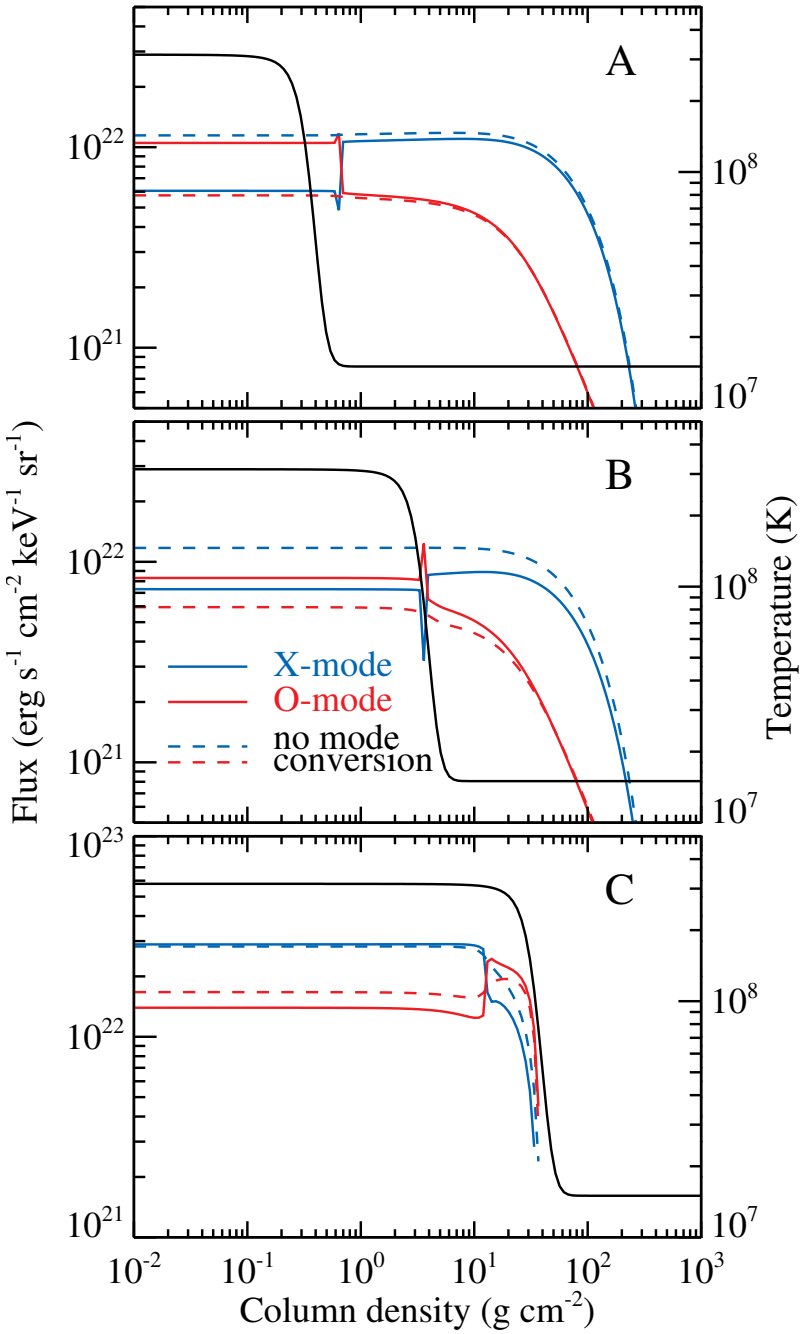

Extended Data Figure 6. Flux emergent from the heated layer in two polarization modes. Distributions of the fluxes in two polarization modes, X and O, as a function of the column density at photon energy of 5.1 keV are shown with blue and red curves for the three models with $m_{\rm up} = 0.3, 3$, and 30 g cm^{-2} in panels **(A)**, **(B)**, and **(C)**, respectively. Models with and without mode conversion at the vacuum resonance are shown with the solid and dashed curves, respectively. The corresponding temperature distributions are shown with the black curves (right axes).

X-mode dominates. Note that the depth of the transition layer of $m_{\rm up} \approx 3\,{\rm g\,cm^{-2}}$ appears to be natural as it corresponds to the optical depth of around unity, where the free-free cooling becomes inefficient while the Compton cooling becomes important. The radiation escaping the atmosphere can be dominated by the O- or X-mode, depending on the exact value of $m_{\rm up}$ and the detailed temperature structure. The polarization mode can also depend on the angle between the surface normal and the direction of photon propagation. At energies a factor of 10 below the electron cyclotron energy, the vacuum polarization dominates at the outer overheated layer. As a result, both modes are nearly linearly polarized at zenith angles larger than $\sim 6^\circ$ and therefore in a broad angle range the PD can be computed as the ratio of the difference in the intensities of the two modes to their sum[55]. As an illustration, we show in Extended Data Figure 5C the PD as observed at different zenith angles for $m_{\rm up} = 3\,{\rm g\,cm^{-2}}$. We see that at very small and very large inclination the PD is negative (i.e. the X-mode dominates), while at intermediate angles the PD is positive (i.e. the O-mode dominates). This indicates that mixing of radiation observed from different emission regions (i.e. at different angles) can lead to depolarization. We cannot confidently state that the suggested process is responsible for the low polarization of the observed radiation from Her X-1, but it can be potentially important for the final accurate model and for the interpretation of the low polarization signal from other X-ray sources, e.g., magnetars.